Carbon 200 (2022) 1–9

Contents lists available at ScienceDirect

Carbon

journal homepage: www.elsevier.com/locate/carbon

Intercrystallite boundaries dominate the electrochemical corrosion behavior of polycrystalline diamond

Chen Xiao [a,b], Fiona Elam [a,b], Stefan van Vliet [a], Roland Bliem [a], Simon Lépinay [b], Noushine Shahidzadeh [b], Bart Weber [a,b], Steve Franklin [a,c,*]

[a] Advanced Research Center for Nanolithography (ARCNL), Science Park 106, 1098XG, Amsterdam, the Netherlands
[b] Van der Waals-Zeeman Institute, Institute of Physics, University of Amsterdam, Science Park 904, 1098XH, Amsterdam, the Netherlands
[c] Department of Materials Science and Engineering, The University of Sheffield, Sheffield, S13JD, UK

A B S T R A C T

In this work, high resolution integrated AFM–EC/SECM was used to reveal the spatially heterogeneous electroactivity of microcrystalline diamond (MCD) and nanocrystalline diamond (NCD) surfaces. During electrochemical corrosion, NCD surfaces undergo a stronger corrosion reaction than MCD because of the higher amount of sp^2 hybridized carbon. In-situ EC-AFM imaging shows no significant change in surface morphology, while corroded surfaces become more hydrophilic due to the oxidation reactions that occur in the outermost layer. On non-corroded MCD and NCD surfaces, intercrystallite boundaries exhibit stronger localized (electro) chemical reactivity than crystallites. However, after electrochemical corrosion, both MCD and NCD surfaces become thermodynamically stabilized by corrosion products that passivate the surface and inhibit further corrosion. In this way, the (electro)chemical reactivity of the intercrystallite boundaries is reduced to a greater extent by electrochemical corrosion than the (electro)chemical reactivity of the crystallites due to the more intense electrochemical oxidation reactions taking place at these boundaries. After corrosion, this results in a comparatively greater (electro)chemical reactivity on the crystallites than at the boundaries. This behavior suggests the following order of (electro)chemical reactivity: $sp^2 > sp^3 >$ oxidized/passivated structures.

1. Introduction

Polycrystalline diamond is an attractive candidate for devices that need to withstand a variety of harsh environments over long periods of operation. The development of chemical vapor deposition technology now enables diamond films to be used for a variety of extreme wear and corrosion applications such as orthopedic artificial joint prostheses and heart valves in the human body (body fluid condition) [1–3], mechanical seals and bearings in marine ships (salt water) [4], nanodes, and nanoelectrode arrays in electrochemical biosensor applications (aqueous solutions) [5–7]. Although the diamond films used in these applications are chemically very inert, the terminated groups, surface topography and chemical properties at the surface can change when exposed to electrolyte solutions for long periods, which can affect the serviceability of the surface or even lead to application failure. The evolution of the localised chemical and electrochemical properties of diamond films is therefore of significance, to the prediction of life expectancy and the exploration of failure mechanisms, in long-term applications in corrosive media such as body fluid and salt solutions.

A polycrystalline diamond film is a two-phase system composed of largely sp^3-hybridised diamond crystallites and intercrystallite boundaries. The latter are thought to be composed of sp^2-graphitic carbon, amorphous carbon, and CH_x, and may display similar properties to diamond-like carbon (DLC), which contains different fractions of amorphous carbon (sp and sp^2 hybridisation) and diamond carbon bonds [8,9]. Since amorphous carbons are generally more conductive and chemically oxidizable than crystalline diamond carbon, the chemical corrosion rate is higher, especially for sp^2-compared to sp^3-hybridised carbon [10,11]. Using X-ray photoelectron spectroscopy (XPS) and Raman spectroscopy, previous corrosion studies with DLC showed that corrosion takes place predominantly via a reduction in the carbon sp^2 content, resulting in the formation of oxides of C═O, C–OH, C–O and C(=O)–OH [12–15]. This also indicates that the carbon sp^3 fraction of DLC plays a key role in its corrosion resistance. It is believed that as-grown diamond crystallites carry hydrocarbon groups (C–H); whereas oxidized intercrystallite boundaries, either ether (C–O–C) or carbonyl (C═O) groups [16]. In some studies, amorphous carbon has been used as a model substance for the intercrystallite boundaries of heterogeneous polycrystalline diamond surfaces to investigate the electrochemical properties and chemical reactivity of such intercrystallite boundaries. However, it has been reported that there is still a large difference in chemical composition and structure between

* Corresponding author. Advanced Research Center for Nanolithography (ARCNL), Science Park 106, 1098XG, Amsterdam, the Netherlands.
E-mail address: s.franklin@arcnl.nl (S. Franklin).

https://doi.org/10.1016/j.carbon.2022.08.038
Received 13 May 2022; Received in revised form 26 July 2022; Accepted 8 August 2022
Available online 17 August 2022

amorphous carbon and real polycrystalline diamond boundaries [17]. Localized surface chemistry changes, including surface termination and structure reconstruction, strongly affect the electro(chemical) reactivity, and are especially relevant for the complex electrochemical corrosion behavior of a polycrystalline diamond surface due to the non-uniform surface structure.

The main challenge with elucidating the corrosion behavior at the intercrystallite boundaries of polycrystalline diamond films is spatial resolution. Characterization methods including electrochemical atomic force microscopy (EC-AFM), X-ray photoelectron spectroscopy (XPS), and Raman spectroscopy can only be used to assess the electrochemical/chemical behavior over large areas; detailed localized information on the individual diamond crystallites and intercrystallite boundaries cannot be obtained with such techniques. Yet, such local information on the electrochemical behavior of synthetic diamond is needed to make next steps in the development of applications of the coating. Scanning electrochemical microscopy (SECM) is an advanced technique that can be used to measure the localized electrochemical behavior at liquid/solid interfaces. Previous SECM studies have provided insight into the influence of diamond dopant levels, defects and impurities on the electroactivity [18–24]. However, these experiments have not yet revealed what the relative importance of the intercrystallite boundaries and the crystallite faces is, in determining the overall electrochemical stability of the coating. The main experimental challenges that need to be overcome in order to address this question is the limitation in electrode tip size and the use of conductive coatings. Both of these make localized measurements difficult, thereby hindering our ability to identify and resolve failure mechanisms of the coating.

In this study, microcrystalline diamond (MCD) and nanocrystalline diamond (NCD) with different fractions of intercrystallite boundaries were compared in order to elucidate the influence of the crystal structure on (electro)chemical kinetics and thermodynamics. In-situ EC-AFM was used to characterize the surface topography evolution and electrochemical responses of the polycrystalline diamond surfaces before and after electrochemical corrosion. By using an ultramicroelectrode (UME) tip with a radius of curvature of 25 nm in SECM, we were able to resolve the conductivity and electrochemical reactivity of the diamond coatings at the crystallite level. In addition, ex-situ XPS and Raman spectroscopy were used to examine the effect of corrosion on the surface chemistry and structural evolution of MCD and NCD films. Our results show that intercrystallite boundaries are more susceptible to corrosion than crystallites and dominate the electrochemical reactivity changes of polycrystalline diamond in electrochemical corrosion.

2. Experimental

2.1. Materials

In order to exclude the influence of doping elements on the chemical and electrical properties of the diamond surface, and to avoid uncertainties regarding the homogeneity of the surface elements, undoped MCD and NCD films produced by Advanced Diamond Technologies (Romeoville, USA) with a thickness of 1 μm, synthesized by hot filament CVD on a single crystal N-type silicon substrate with a square area of 40 × 40 mm^2, were adopted as the working electrodes in all electrochemical tests. The resistances of the diamond films and Si substrate were estimated at 5×10^6 Ω and 1×10^3 Ω respectively using impedance spectroscopy. The (root mean square, RMS) surface roughness and grain size of non-corroded diamond films were measured in tapping mode by atomic force microscopy (AFM) to be approximately 13.2 nm and 400–500 nm for MCD, and 10.4 nm and 50–100 nm for NCD respectively, over a square scanned area of 2 μm × 2 μm using a sharp Si AFM tip with a nominal diameter of approximately 20 nm. The sample surfaces were cleaned by chemically pure ethanol (Sigma Aldrich) and subsequently deionized water, and dried using pure N_2 gas before carrying out the electrochemical tests and chemical characterizations.

2.2. Electrochemical and topographical investigations

All electrochemical and topographical experiments were performed at room temperature (22 °C). As shown in Fig. 1a–c, the MCD and NCD samples are mounted in an AFM-compatible electrochemical cell module (Dimension Icon, Bruker, MA, USA): the diamond-coated side was maintained in contact with two gold-plated spring pins that provided the electrical connection with the working electrode. A circular area of 35 mm diameter on the sample surface was exposed to an electrolyte solution of 0.1 M potassium chloride (KCl, Sigma Aldrich) for different corrosion durations and a fluorine rubber O-ring was used to seal the gap between sample clamp and sample [25]. Open circuit potential (OCP) and chronoamperometry measurements were performed using an electrochemical workstation with a bipotentiostat (CHI 760E, CH Instruments, TX, USA). Ag|AgCl and Pt wires served as the reference and counter electrodes respectively and all potentials are given with reference to the reference electrode (Ag|AgCl in 0.1 M KCl). Prior to corroding the diamond films, an OCP test was carried out for more than 15 min until the variation of voltage was within ±0.001 V. An anodic (oxidative) potential range of 0.5–2.5 V was applied to evaluate the effect of corrosion on surface topography and electrochemical response of the MCD and NCD samples.

2.3. SECM tests on non-corroded and corroded MCD and NCD

A schematic of the SECM set-up is given in Fig. 1d. In all SECM tests, the samples were immersed in a solution of 0.01 M Hexaammineruthenium(III) chloride ($Ru(NH_3)_6Cl_3$, which is a nearly ideal outer-sphere redox agent that is insensitive to most surface defects or impurities, in 0.1 M KCl [26]. An ultramicroelectrode (UME) attached on a cantilever with a spring constant of 1.5 N/m was then used to scan horizontally above the MCD and NCD samples, both in the non-corroded condition and after 2.5 h of electrochemical corrosion at an applied voltage of 2.5 V in 0.1 M KCl electrolyte solution. More details regarding the UME tip can be found in Fig. S1 in the Supporting Information. The tip current is measured, which is derived from the electron transfer during the redox reactions between $[Ru(NH_3)_6]^{3+/2+}$ and the PCD substrate performed at −0.7 V versus Ag/AgCl. An UME measures a steady-state, diffusion-limited, current in bulk solution. As the UME approaches the sample surface, the current strongly depends on the tip-sample distance and the sample surface conductivity. As shown in Fig. 1e and f, when the UME probe approaches an insulating surface, diffusion to the probe of the chemical species involved in the redox reaction becomes increasingly hindered. This leads to negative feedback behavior: a decrease in current with decreasing tip-sample distance. The rate at which tip current decreases with decreasing tip-sample distance reflects the surface reactivity. On the contrary, with a conductive sample surface, biased at a potential that allows for regeneration of $[Ru(NH_3)_6]^{3+}$, the increased local concentration as the UME probe approaches the surface results in positive feedback behavior and a current increase with reduced tip−sample distance. In this case, a higher rate of change of current as the probe approaches the sample surface indicates a lower surface reactivity. In AFM-SECM, two-step interleaved scan mode is generally used. In the first step the AFM information, e.g., topography, and the redox reaction current, are mapped in a first scan at a tip-sample distance of 0 nm with the force setpoint of approximately 30 nN. During the subsequent lift scan, the UME follows the mapped surface topography at a constant lift height of 100 nm. By recording the electrochemical response of the tip at different scanning locations, the heterogeneity in electrochemical activity of the sample surface is imaged [27]. This complex interpretation of the SECM results is summarized in Table S1. The scanned size of the AFM-image was 2 μm × 2 μm for the surface topography and electrochemical mapping. Note that due to the expected significant influence of surface roughness on the SECM results, where the area from which the information on current is gathered from a much smaller area than in EC-AFM, it is not possible to

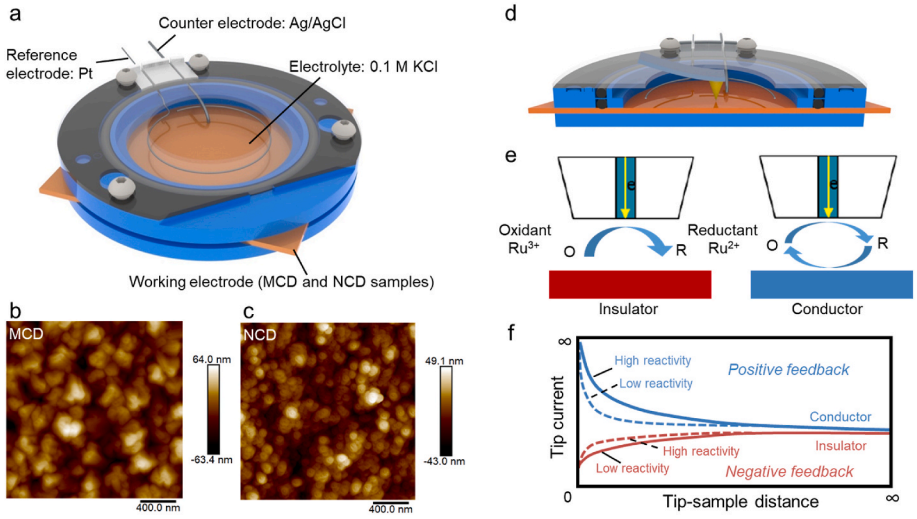

Fig. 1. (a) Schematic of AFM-EC/SECM. AFM images of non-corroded (b) MCD and (c) NCD samples, scanned by a sharp Si tip with a diameter of 20 nm. (d) Cutaway view of the SECM module equipped with an EC-AFM setup. (e) Illustration of the SECM feedback mode over an insulating substrate (left, negative feedback) and conducting substrate (positive feedback, right). The redox reaction of the $Ru(NH_3)_6Cl_3$ agent is $[Ru(NH_3)_6]^{3+} \leftrightarrows [Ru(NH_3)_6]^{2+} + e^-$. (f) Typical approach curves for a nanoelectrode probe on an insulating substrate (red) and on a conducting substrate (blue). (A colour version of this figure can be viewed online.)

use this technique to quantitatively compare the localized (electro) chemical reactivity of MCD and NCD surfaces. Therefore, in this study, only the (electro)chemical reactivity of the crystallites and intercrystallite boundaries on the same MCD or NCD surface could be contrasted by SECM mapping. To avoid tip contamination, a pre-treatment and cleaning process was performed on the UME and details of this procedure can be found in the Supporting Information.

2.4. Chemical characterization by XPS and Raman

To determine the effect of electrochemical corrosion on the chemical composition and atomic structure of the diamond surfaces, XPS (HiPP-3 Analyzer (entrance slit 1.0 mm), Scienta Omicron, Taunusstein, Germany) and Raman spectroscopy (WITec UHTS 300, Ulm, Germany) were performed on non-corroded and corroded MCD and NCD surfaces. The XPS analyses were performed on a HiPP-3 spectrometer with a 0.8 mm cone and a slit setting of 1.0 mm using a monochromatic Al Kα source. The base pressure was below 1×10^{-9} mbar, and operating pressure below 5×10^{-9} mbar. Data analysis was performed using KolXPD. Atomic ratios were calculated from spectra acquired at a pass energy of 300 eV and corrected for the respective photoemission cross sections. The C 1s high resolution spectra were acquired at a pass energy of 100 eV. The fitting parameters used in the deconvolution of the C 1s spectra of the MCD and NCD surfaces are displayed in Table S2. To accurately locate the peak position of C 1s and exclude shifts due to surface charging, an Au film with a thickness of ~2 nm was deposited on the diamond surfaces. The binding energies were referenced to the Au 4f5/2 peak (84 eV). The typical Raman spectra of the MCD and NCD surfaces measured by a 532 nm excitation laser and exhibit a well-defined peak at 1332 cm^{-1}, which is associated with ordered or crystalline diamond (sp^3 hybridization), and a broad peak in the 1500 cm^{-1} region (sp^2 hybridization), which is composed of a D peak at 1350 cm^{-1} (disordered

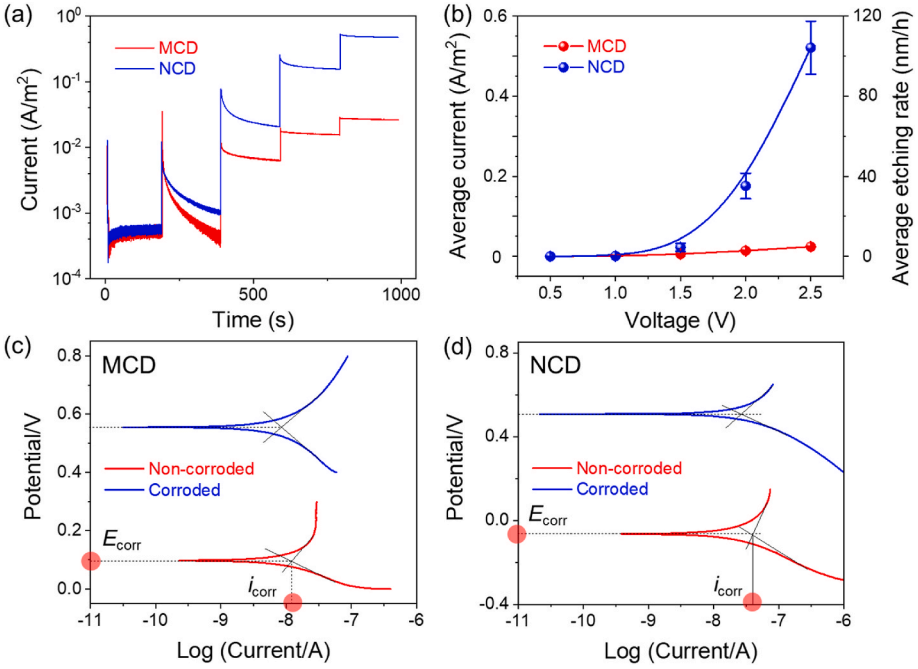

Fig. 2. (a) Measured corrosion current plotted as a function of applied voltage and time. (b) Average etch rate calculated over the cycle area with a diameter of 3.5 cm using equation (1). Tafel extrapolation of polarization curves measured on MCD (c) and NCD (d) surfaces before and after 2.5 h electrochemical corrosion in 0.1 M KCl solution with 2.5 V. (A colour version of this figure can be viewed online.)

carbon) and a G peak at 1580 cm^{-1} (graphitic carbon) [28,29].

3. Results and discussion

3.1. Electrochemical properties of MCD and NCD

Before electrochemical tests, the initial OCP for non-corroded MCD and NCD samples was measured as ~0.2 V and ~0.1 V, respectively. Fig. 2a displays the measured corrosion current evolution of MCD and NCD as a function of corrosion time, and Fig. 2b the average current values for the five applied voltages of 0.5–2.5 V in increments of 0.5 V. The NCD sample shows a higher corrosion current than MCD, especially at high anodic potentials. According to Ohm's law, the more conducting the electrode material, the higher the current for the same potential. In this case however, no obvious difference between the currents of the MCD and NCD samples could be observed at applied anodic potentials lower than 1 V. This is expected, for a current that is limited by carbon corrosion reactions [30]. When the potential is increased above 1 V, a large difference is observed between the measured currents in the chronoamperometry tests for MCD and NCD, indicating that the different currents of the MCD and NCD samples are not caused by different sample conductivity but by different electrochemical corrosion kinetics. The NCD surface is subjected to more intense electrochemical corrosion than the MCD surface, which can be attributed to the greater area of intercrystallite boundaries with the less chemically stable sp^2 hybridization structure. Considering the structurally and compositionally heterogeneous polycrystalline diamond surfaces, the value of the current does not reflect localized electrochemical properties but reflects the total corrosion rate of the exposed area of 9.6 cm^2. To enable a comparison with the corrosion rate reported in previous literature, the average current values can be converted to average electrochemical corrosion rates based on the following equation (1) [31],

$$\text{Corrosion rate} = Mj_{corr}/\rho zF \quad (1)$$

where j_{corr} is the current density (A/cm^2), M and ρ are the molar mass (g/mol) and density (g/cm^3) of corroding species, z is the number of electrons involved in electrochemical reaction, and F is Faraday constant. On this basis, the electrochemical corrosion rate of MCD and NCD can be estimated at 2.5 nm/h and 104.1 nm/h, respectively, based on the parameters of single crystal diamond.

The electrochemical corrosion thermodynamics and kinetics of the materials can be evaluated by adopting Tafel Extrapolation of potentiodynamic polarization. From the Tafel analysis, the OCP or corrosion potential (E_{corr}) and corrosion current density (I_{corr}) can be estimated [32]. Fig. 2c and d displays the anodic (for low potential, $E \leq E_{corr}$) and cathodic (for high overpotential, $E > E_{corr}$) polarization curves for MCD and NCD before and after 2.5 h of electrochemical corrosion with the applied voltage of 2.5 V immersed in 0.1 M KCl electrolyte solution. After electrochemical corrosion, the value E_{corr} increases from 0.1 V to 0.55 V for the MCD sample and from −0.05 V to 0.5 V for the NCD sample, but I_{corr} decreased from 12 nA to 8 nA for the MCD sample and from 39 nA to 27 nA for the NCD sample. This indicates that oxidized MCD/NCD surfaces are thermodynamically more stable than non-oxidized (pristine) surfaces, which may be attributed to the inhibiting effect of corrosion products (terminated surface or oxidized topmost layer) forming and covering the surface during the electrochemical corrosion process. Moreover, the NCD surface displays a higher corrosion tendency (lower OCP) and higher corrosion rate than the MCD surface, in both non-corroded and corroded cases. Furthermore, the change in E_{corr} for the NCD before and after electrochemical corrosion (+0.55 V) is also greater than that for the MCD (+0.45 V). This difference suggests that the larger area of the intercrystallite boundaries in NCD leads to a much more prominent oxidation reaction and surface change during electrochemical corrosion, relative to MCD [33].

As the chronoamperometry measurement was performed using EC-AFM, the surface topography at the microscale could be imaged in-situ as a function of the electrochemical corrosion duration. Fig. S2 shows AFM images obtained on MCD and NCD surfaces after different corrosion durations in 0.1 M KCl electrolyte solution, together with the surface roughness (RMS value) plotted as a function of electrochemical etching time. No obvious difference between the surface topography of non-corroded and corroded surfaces was observed. PCD is thermodynamically more stable than DLC, which shows extensive pitting corrosion on the corroded coating surface using the same electrochemical set-up and conditions [12]. However, the water contact angle of both MCD and NCD surfaces was shown to decrease significantly, demonstrating that the surfaces had become more hydrophilic after 2.5 h electrochemical corrosion (Fig. S3). The water contact angle measurements were made under macroscopic conditions and therefore correspond well to the results of Fig. 2. These results show that the predominant effect of the electrochemical corrosion process is to alter the surface chemistry of the topmost layers of the diamond films, through oxidation, without changing the surface topography.

3.2. Chemical characterizations of MCD and NCD before and after electrochemical corrosion

The Raman spectra obtained from the MCD and NCD films before and after 2.5 h electrochemical corrosion are given in Fig. 3a and are composed of several typical signature peaks. The sp^3-related phonon band at ~1333 cm^{-1}, which occurs in single crystal diamond, could be clearly distinguished in the spectra of the non-corroded and corroded MCD films but was much less prominent in the NCD spectra. The difference in width of this band compared with the single crystal diamond Raman spectrum is a good indicator of crystallinity and purity, and Fig. 3a indicates that electrochemical corrosion had little influence on this [27]. The much larger full width at half maximum of the 1333 cm^{-1} band on the MCD surface (~10 cm^{-1}) compared with that of a single crystal diamond spectrum (~2 cm^{-1}), indicates the presence of crystal defects. The slight deviation compared to the reference value (1332 cm^{-1}) is an indication of residual stresses within the coating [34]. Compared to MCD, the 1333 cm^{-1} band for NCD films is barely visible because of the asymmetry and broadening of the diamond peak caused by phonon-related interaction [35]. The two peaks at ~1140 cm^{-1} and ~1480 cm^{-1}, displayed in both MCD and NCD surfaces, come from the scattering of *trans*-polyacetylene (TPA) oligomers and are assigned to C–H bending and C–C stretching modes of TPA chains, respectively. The broad humps at ~1360 cm^{-1} and ~1560 cm^{-1} are constituted mainly by the D and G bands respectively, and are due to the sp^2/a-C phases concentrated at the intercrystallite boundaries [36,37]. The presence of the D peak indicates the existence of aromatic sp^2 rings, whereas the G peak can arise from sp^2-C in both rings and chains. Since the signal detected by Raman spectroscopy represents material information from a relatively large penetration depth of ~1 μm, chemical changes resulting from electrochemical corrosion occurring in the outermost layer are not readily revealed by Raman spectra. As shown in Fig. 3a, only minimal differences between corroded and non-corroded material were exhibited by the Raman spectra except for a small increase in the D band region after 2.5 h electrochemical corrosion.

The 1333 cm^{-1} peak results from the first-order phonon associated with the sp^3 diamond lattice, whereas the closely adjacent D band region with a peak at 1360 cm^{-1} indicates disorder in the sp^2 structure of graphitic carbon. The 1333 cm^{-1} intensity relative to the 1360 cm^{-1} band is used extensively to evaluate the relative amounts of sp^3 and sp^2 hybridized carbon. The spectra were de-convoluted into Gaussian lines and the sp^2/sp^3 bonds ratio (~0.28 and ~0.58 for non-corroded MCD and for NCD samples, respectively, and increase slightly after electrochemical corrosion) can be found in Fig. S4. The slight increase in the sp^2 signal for corroded diamond surfaces is the result of a competition between different effects. Electrochemical corrosion and oxidation reactions occurring on the diamond crystal surfaces lead to disruption of

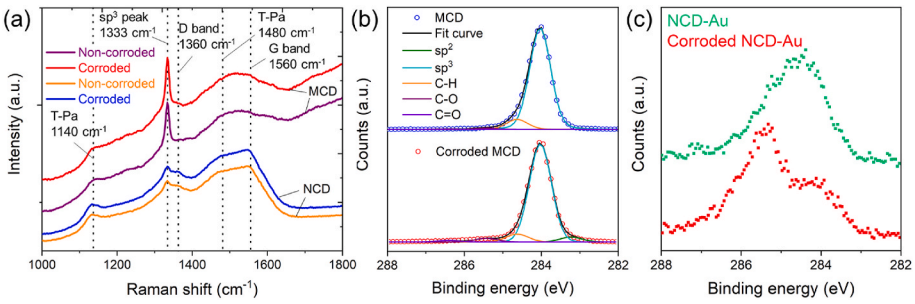

Fig. 3. (a) Raman spectra of non-corroded and corroded MCD and NCD. The electrochemical corrosion duration of 2.5 h was performed on MCD and NCD surfaces in 0.1 M KCl electrolyte solution with the applied voltage of 2.5 V. (b) High resolution C 1s spectra of pristine MCD (green circle) and corroded MCD (red square) with peak fitting of sp^2, sp^3, C–H, C–O, and C═O. (c) High resolution C 1s spectra of pristine NCD-Au (green circle) and corroded NCD-Au (red square). (A colour version of this figure can be viewed online.)

the sp^3 structure and an increase in the fraction of sp^2 structure, while reactions occurring at the intercrystallite boundaries might result in a reduction in the sp^2 content. In addition, electrochemical corrosion of polycrystalline films results in surfaces that are passivated by the formation of oxidized species on the surface with a lower corrosion rate and a higher thermodynamic stability (see in Fig. 2c and d) [38].

To determine qualitatively the effect of the corrosion of MCD on the chemical composition of its topmost nanometers, XPS was performed on non-corroded and corroded MCD. Table 1 displays the elemental composition of the surface region measured using XPS. A detailed XPS examination of the C 1s spectra of non-corroded MCD and corroded MCD can be seen in Fig. 3b. The resulting quantification of the carbon species is shown in Table 2, where the analysis takes into account the reported binding energy shifts in diamond due to band bending [39]. Upon corrosion, an increase in oxygen, silicon, and chlorine species is evident. The presence of chlorine is likely due to small amounts of surface contamination from the KCl electrolyte used in the EC-AFM cell. The peak positions observed in the Si 2p spectra given in Fig. S5 indicate that the silicon is in the form of silicon carbide SiC. The silicon may originate from the silicon wafer substrate or from contamination on the surface [40]. Consequently, the increase in oxygen is most likely attributable to oxidization of the diamond surface. The above ex-situ XPS data fully supports the interpretation given earlier based on AFM topography and EC measurements: a thin surface layer of carbon is oxidized upon exposure to a corrosive environment. Regarding the NCD surface, the greater increase in the oxygen ratio observed for the corroded NCD (Table 1) suggests that the NCD was more strongly oxidized than the MCD under the same electrochemical conditions. In the detailed C 1s spectra (Table 2) both lower (sp^2) and higher (C–O, C═O) binding energy species were observed after corrosion, where the peaks were assigned according to the model in Ref. [39]. The presence of these species indicates the formation of sp^2-type and oxidized carbon species from the corrosion process and corresponds with observations in the literature [12,41].

The effect of electrochemical corrosion on the surface of NCD has also been analyzed with XPS. The non-corroded and corroded NCD samples were coated with a thin layer of gold before the XPS measurement to provide a binding energy reference. These samples are referred to as NCD-Au in Fig. 3c, which shows the detailed C 1s XPS spectra of NCD-Au and corroded-NCD-Au. With the NCD, the peaks are much broader and less well-defined than with the MCD, probably as a result of the finer crystalline structure. Unfortunately, this degree of peak broadness does not provide sufficient basis for a reliable interpretation by peak fitting, which was possible with the MCD. In the detailed spectra of NCD-Au, one broad peak (283–286.5 eV) is visible, exceeding the full-width at half maximum of MCD by a factor of 1.7. The corroded-NCD-Au shows a double-peak, with one component at a comparable binding energy to NCD-Au and the second one at a significantly higher binding energy (approximately +1.4 eV), which is typically assigned to C–O bonds. Using the same peak fitting parameters as those used for MCD results in an unrealistically large calculated value for the percentage of carbon oxide species, which cannot be explained by the total oxygen species present (C–O:O = 9). We attribute the high-binding energy species in the NCD samples to Fermi-level-pinning on the surface of diamond. In this phenomenon, defects at the surface form electronic states in the gap of an insulator and thus locally define its Fermi level. As a result of the localized electronic states, downwards band bending occurs, resulting in a shift of the core level XPS spectra to higher apparent binding energies. Fermi level pinning and band bending have been reported to cause a shift of up to 1.4 eV in experiments introducing surface defects to diamond by oxidation and Ar ion bombardment [42,43], and have even been proposed as the cause for the large variations in the reported C 1s binding energies for diamond [44]. The extreme broadness of the peaks potentially originates from different types and concentrations of defects in the individual NCD crystallites, leading to a distribution of binding-energy shifts and making it impossible to reliably fit the detailed C 1s spectra of our NCD samples. Compared to MCD, the smaller crystallites of the NCD are more susceptible to the effect of surface defects and therefore to defect-induced band bending.

Table 1
Atomic ratios relative to C 1s determined by XPS of NCD, NCD-corroded, MCD, and MCD-corroded.

	C	O	Si	Cl
MCD	100%	3.9%	2.5%	0.0%
Corroded MCD	100%	8.4%	2.7%	0.2%
NCD	100%	2.5%	0.2%	0.0%
Corroded NCD	100%	10.8%	1.3%	0.5%

Table 2
XPS fitting results resolving the C 1s species in MCD and MCD-corroded [39].

	sp^2	sp^3	C–H	C–O	C=O
MCD	0.0%	89.8%	8.9%	1.0%	0.2%
Corroded MCD	4.2%	84.6%	6.8%	3.1%	1.4%

3.3. *Local electrochemical behavior characterized by scanning electrochemical microscopy*

The above results strongly suggest that the electrochemical activity and corrosion rate of the NCD surface are higher than those of the MCD due to the greater density of intercrystallite boundaries. Thus, electrochemical corrosion brings greater changes to the NCD surface compared to MCD. Considering the heterogeneous structure of polycrystalline diamond, the EC-AFM results are not able to provide full details of the electrochemical responses of different structures on the surface. For this reason, high resolution SECM was performed on the diamond surfaces before and after electrochemical corrosion, using an UME with a radius of ~25 nm. Fig. 4a–f display the surface topography (a, d), tip current in near-contact condition (b, e), and tip current in lift mode at a height of 100 nm (c, f) of MCD in a mixed solution of 0.01 M $[Ru(NH_3)_6]^{3+/2+}$ and 0.1 M KCl before and after 2.5 h electrochemical corrosion in 0.1 M KCl electrolyte solution. The tip current, which -as explained previously-is derived from the electron transfer during the redox reactions between

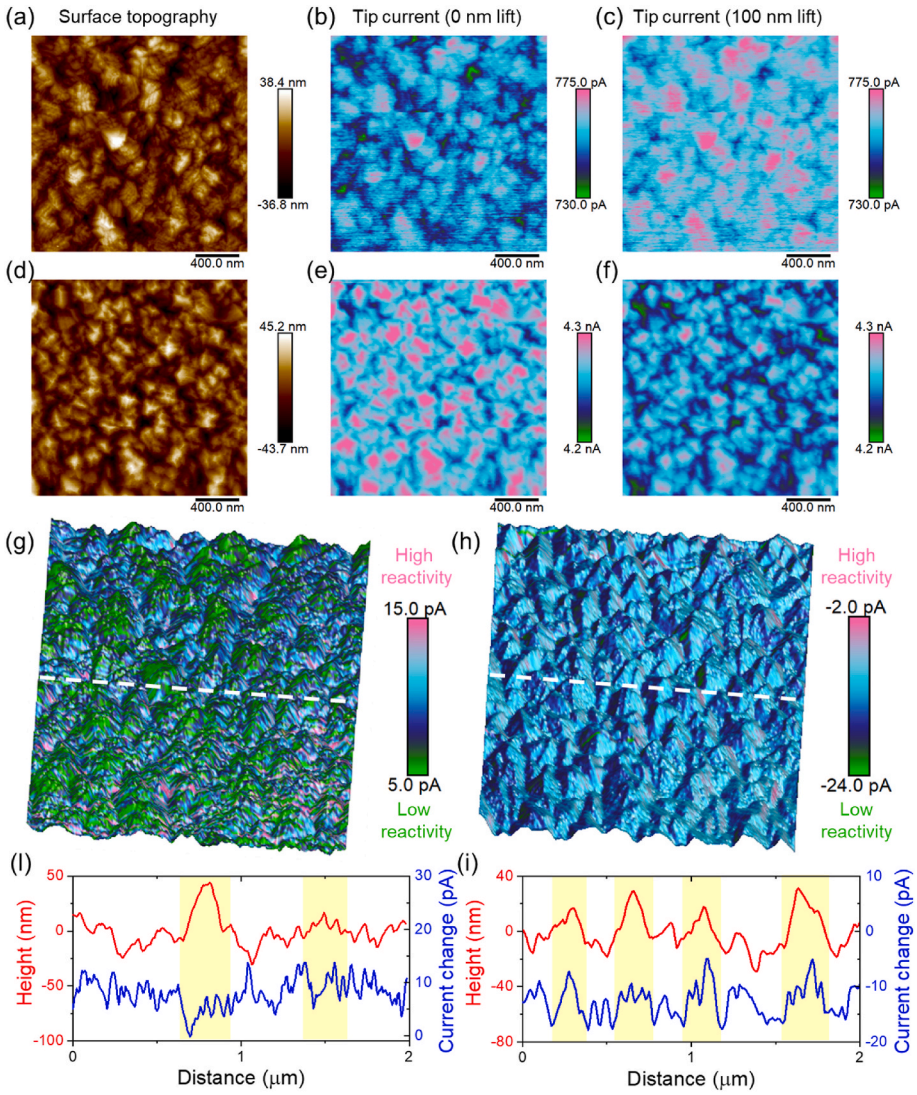

Fig. 4. PeakForce SECM images recorded on 2 μm × 2 μm non-corroded MCD surface (a–c) and corroded MCD surface (d–f) in 10 mM $[Ru(NH_3)_6]^{3+}$ and 0.1 M KCl. (a, d) Surface topography. (b, e) Tip current of PeakForce tapping scan mode when the tip is in contact with the surface. (c, f) Tip current of lift scan mode when the tip-surface distance is controlled at 100 nm by following the surface topography obtained during the Peakforce tapping scan. The current scale for the map obtained in 0 nm and 100 nm lift conditions is the same. Computed difference in current maps obtained from 100 nm and 0 nm lift and superimposed onto AFM topography images (a, d): non-corroded MCD (g) and corroded MCD (h). Typical profiles of surface topography (red line) and current change (blue line) of non-corroded MCD (l) and corroded MCD (i) obtained along the white dashed lines in (g) and (h). (A colour version of this figure can be viewed online.)

$[Ru(NH_3)_6]^{3+/2+}$ and the diamond substrate, follows the topography, and Fig. 4 shows that the SECM system has sufficient accuracy to discriminate between the intercrystallite boundaries and crystallites. The absolute values of the measured current are influenced by the local conductivity of the surface and the local solution environment and therefore do not themselves provide definitive information on the surface chemical reactivity. However, the latter can be characterized by measuring the change in the steady-state diffusion-limited current feedback, which is sensitive to tip-sample distance variations. For the non-corroded MCD surface (Fig. 4a–c), as the tip-sample distance increases from 0 nm lift to 100 nm lift, the average tip current increases (the areas of the light blue and pink regions have increased), reflecting negative feedback behavior. It is important to note that this behavior is not related to bulk material conductivity, but is related to the properties of the outermost layer of the localized area affected by the probe. On the corroded MCD surface (Fig. 4d–f), the tip current decreases as the tip-sample distance increases (the areas of the light blue and pink regions decrease), indicating positive feedback behavior after electrochemical corrosion.

For surfaces with similar surface conductivity, the magnitude of the change in current as a function of tip-sample distance characterizes the chemical (redox) reactivity of the localized area where the UME is located. As explained in section 2.2 and summarized in Table S1, the significance of the rate of change of current with tip-sample distance is different for surfaces displaying negative and positive feedback behavior. For negative feedback, a greater difference in current between 0 and 100 nm tip-sample distance indicates higher surface reactivity, whereas with positive feedback this would indicate a lower surface reactivity. Fig. 4g and h, for MCD, shows plots of the current differentials between the values measured at tip-sample distances of 0 nm and 100 nm superimposed onto the corresponding AFM topography image (Fig. S6). On the non-corroded MCD surface, the highest reactivity regions (pink and light blue areas) occur predominantly between the crystallites, i.e. at the intercrystallite boundaries. However, on the corroded MCD surface, which now displays a positive feedback behavior, the highest reactivity (for positive feedback the smallest decreases in current) occurs on the crystallites. Figs. 4l and i displays, as two-dimensional line-scans through the data, the typical current differential variation (blue line) and surface topography (red line) obtained at the positions shown by the dotted white lines in Fig. 4g and h on non-corroded MCD (l) and corroded MCD (i) surfaces. It is clear that, although the 25 nm radius of the SECM tip results in some filtering-out of signal peaks and valleys, large height locations (crystallites, yellow shadow regions) tend to show low current differentials on the non-corroded surface, while the crystallite locations on the corroded surface show large current differentials. The intercrystallite boundaries, which are expected to be largely composed of sp^2 hybrid and amorphous carbon structures, are more susceptible to corrosion than the crystallites

themselves, which consist predominantly of sp^3 structure. Such oxidation reactions on diamond films are similar to a deep anodic reaction (in acid electrolyte) and thermal treatment in air at 300 °C reported in previous literature [45–47]. Surface termination is usually generated on a diamond surface by electrochemical methods (water reduction to produce H-terminations or oxidation for O-terminations) or plasma treatment (H- and O-terminations) [47–49]. Surface oxidization of a hydrogen-terminated surface causes the surface chemistry to change from hydrogen to oxygen terminated, leading to a decrease in the free carriers concentration, altering the electrochemical behavior from metallic to semiconductor, and decreasing the charge transfer rate for redox couples ($[Ru(NH_3)_6]^{3+/2+}$). As mentioned previously in relation to Fig. 2, after electrochemical corrosion, it is believed that the diamond film surfaces are passivated by hydroxyl groups and thus exhibit greater thermodynamic stability, and that this results in the smaller observed water contact angle. If we assume that any changes in the carbon hybridization on the surfaces of the crystallites are relatively small before and after electrochemical corrosion, or considered negligible relative to changes at the intercrystallite boundaries, the results of the SECM experiments on the spatially heterogeneous surface suggest that the order of chemical (redox) reactivity is as follows: sp^2 > sp^3 > oxidized/passivated structure.

Fig. 5 shows corresponding information for the NCD surfaces. Fig. 5a–f displays the surface topography and 2D maps of the tip current measured at tip-sample distances of 0 nm and 100 nm, before and after electrochemical corrosion of 2.5 h duration. The tip current follows the surface topography, and although the intercrystallite boundaries are not as well defined as with the MCD (which is attributed to the resolution limit of the SECM system), they are still discernible in the images. Both non-corroded (Fig. 5 a-c) and corroded (Fig. 5 d-f) NCD surfaces show a decrease in the average current (smaller and fewer pink and light blue regions) as the tip lift height increases from 0 to 100 nm, indicating that these surfaces display positive feedback behavior. For the non-corroded NCD surface, the current differential map (Fig. 5g), which is superimposed onto the corresponding AFM topography image (Fig. S7), together with the two-dimensional line-scan (Fig. 5l), indicate that the high surface reactivity areas (pink regions) are concentrated around the intercrystallite boundaries rather than on the crystallites themselves. For the corroded NCD, Fig. 5h and i suggest that the highest reactivity occurs on the diamond crystallites rather than at the intercrystallite boundaries. This change in relative reactivity after corrosion is the same as that found with the MCD sample. Thus, although the MCD and NCD samples differ in their area-ratio of intercrystallite boundaries and crystallites, they exhibit a similar trend of diamond structure-dependent local (electro)chemical reactivity. Combining the thermodynamic and kinetic behaviors of electrochemical corrosion before and after corrosion, the same conclusion as that previously found with MCD can be drawn as regards the order of the chemical (redox) reactivity: sp^2 > sp^3

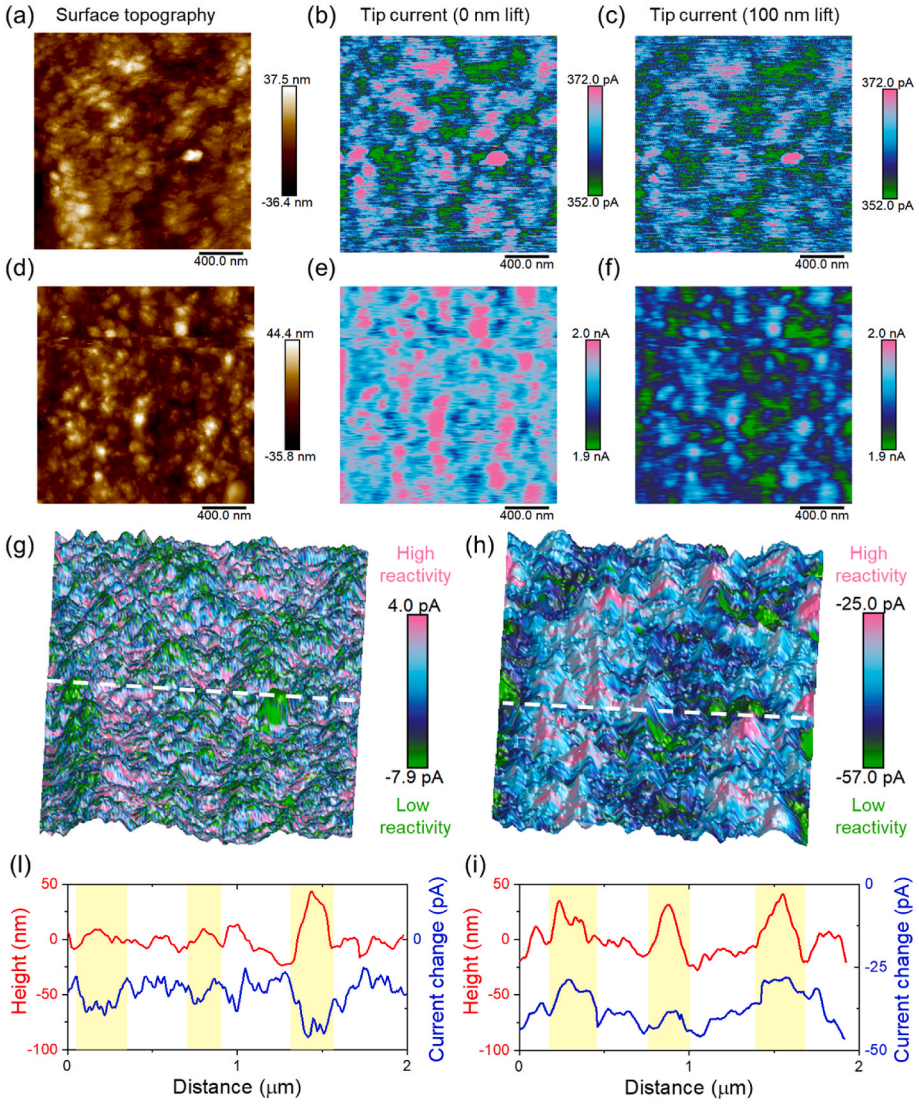

Fig. 5. PeakForce SECM images recorded on 2 μm × 2 μm of non-corroded NCD surface (a–c) and corroded NCD surface (d–f) in 10 mM $[Ru(NH_3)_6]^{3+}$ and 0.1 M KCl. (a, d) Surface topography. (b, e) Tip current of PeakForce tapping scan mode when the tip is in contact with surface. (c, f) Tip current of lift scan mode when the tip-surface distance is controlled at 100 nm by following the surface topography obtained during the Peakforce tapping scan. The current scale for the map obtained in 0 nm and 100 nm lift conditions is the same. Computed difference in current maps obtained from 100 nm and 0 nm lift and superimposed onto AFM topography images (a, d): non-corroded NCD (g) and corroded NCD (h). Typical profiles of surface topography (red line) and current change (blue line) of non-corroded NCD (l) and corroded NCD (i) obtained along the white dashed lines in (g) and (h). (A colour version of this figure can be viewed online.)

> oxidized/passivated structure.

4. Conclusions

In this work, high resolution integrated AFM–EC/SECM using an ultramicroelectrode tip with a radius of 25 nm was utilized to reveal the spatially heterogeneous electroactivity of MCD and NCD surfaces. XPS and Raman surface characterization indicated that oxidation reactions occur on the outermost layer, producing an oxidized diamond layer on MCD and NCD surfaces during electrochemical corrosion. Since the intercrystallite boundary is composed of various sp and sp^2 hybridised carbon species, it has a poorer corrosion resistance and undergoes stronger electrochemical oxidation reactions compared to the diamond crystallite. Thus, intercrystallite boundaries dominate the electrochemical corrosion behavior of polycrystalline diamond. In the electrochemical corrosion process, the NCD surface underwent a stronger electrochemical corrosion reaction than MCD due to the higher intercrystallite boundary component. After electrochemical corrosion, both MCD and NCD surfaces became thermodynamically more stable, which may be attributed to the inhibiting effect of corrosion products generated by the electrochemical oxidization reactions that passivate the surface (i.e., terminated groups and oxidized outermost layer). Because of the greater (electro)chemical reactivity of the intercrystallite boundaries, they are affected more by the passivation effect and, as a consequence, the (electro)chemical reactivity of the intercrystallite boundaries is reduced to a greater extent by electrochemical corrosion than the crystallites. After corrosion, this results in a relatively greater (electro)chemical reactivity on the crystallites than at the boundaries. The above results suggest the following order of (electro)chemical reactivity: $sp^2 > sp^3 >$ oxidized/passivated structures.

The conclusions indicate that, in applications where a high (electro) chemical reactivity needs to be maintained for a long period, such as nanodes, a good balance needs to be found between the competing behaviors of the crystallites and the intercrystallite boundaries, which enhance the electrochemical properties but are not conductive to long-term operation. In contrast, for application scenarios where (electro) chemical inertness is an important requirement, an effective strategy may be to reduce the intercrystallite boundary density by increasing the size of the crystallites, or to pretreat the PCD using an oxidation treatment. Given the complexity of the actual application situations, many important factors such as the concentration and pH value of electrolyte, and the doping concentration and type within the PCD coating, which have not been discussed in this study, should be considered in future research.

Credit author contribution statement

Chen Xiao: Conceptualization, Methodology, Validation, Formal analysis, Investigation, Writing – original draft. **Fiona M. Elam:** Methodology, Formal analysis, Investigation, Writing – review & editing. **Stefan van Vliet:** Formal analysis, Writing – original draft. **Roland Bliem:** Formal analysis, Writing – review & editing. **Simon Lépinay:** Formal analysis, Writing – review & editing. **Noushine Shahidzadeh:** Resources, Writing – review & editing. **Bart Weber:** Writing – review & editing, Funding acquisition. **Steve Franklin:** Conceptualization, Supervision, Formal analysis, Writing – review & editing, Funding acquisition.

Declaration of competing interest

The authors declare that they have no known competing financial interests or personal relationships that could have appeared to influence the work reported in this paper.

Acknowledgements

This work has been carried out at the Advanced Research Center for Nanolithography (ARCNL), a public-private partnership of the University of Amsterdam (UvA), the Vrije Universiteit Amsterdam (VU), the Netherlands Organisation for Scientific Research (now) and the semiconductor equipment manufacturer ASML. We are grateful to Dr. Hartmut W. Stadler (Bruker Corporation, Billerica, United States) for his assistance in the SECM measurements. B.W. acknowledges funding from the NWO VENI grant No. VI.Veni.192.177.

Appendix A. Supplementary data

Supplementary data to this article can be found online at https://doi.org/10.1016/j.carbon.2022.08.038.

References

[1] H.A. Ching, D. Choudhury, M.J. Nine, N.A.A. Osman, Effects of surface coating on reducing friction and wear of orthopaedic implants, Sci. Technol. Adv. Mater. 15 (1) (2014), 014402.
[2] M. Amaral, A. Dias, P. Gomes, M. Lopes, R. Silva, J. Santos, et al., Nanocrystalline diamond: in vitro biocompatibility assessment by MG63 and human bone marrow cells cultures, J. Biomed. Mater. Res. 87 (1) (2008) 91–99.
[3] A.M. Schrand, S.A.C. Hens, O.A. Shenderova, Nanodiamond particles: properties and perspectives for bioapplications, Crit. Rev. Solid State Mater. Sci. 34 (1–2) (2009) 18–74.
[4] B. Lingwall, T. Sexton, C. Cooley, Polycrystalline diamond bearing testing for marine hydrokinetic application, Wear 302 (1–2) (2013) 1514–1519.
[5] C. Dincer, E. Laubender, J. Hees, C. Nebel, G. Urban, J. Heinze, SECM detection of single boron doped diamond nanodes and nanoelectrode arrays using phase-operated shear force technique, Electrochem. Commun. 24 (2012) 123–127.
[6] C. Xiao, F.C. Hsia, A. Sutton-Cook, B. Weber, S. Franklin, Polishing of polycrystalline diamond using synergies between chemical and mechanical inputs: a review of mechanisms and processes, Carbon 196 (2022) 29–48.
[7] S. Daboss, P. Knittel, C.E. Nebel, C. Kranz, Multifunctional boron-doped diamond colloidal AFM probes, Small 15 (48) (2019), 1902099.
[8] O.A. Williams, Nanocrystalline diamond, Diam. Relat. Mater. 20 (5–6) (2011) 621–640.
[9] O.A. Williams, A. Kriele, J. Hees, M. Wolfer, W. Müller-Sebert, C. Nebel, High Young's modulus in ultra thin nanocrystalline diamond, Chem. Phys. Lett. 495 (1–3) (2010) 84–89.
[10] J.J. Tully, E. Braxton, S.J. Cobb, B.G. Breeze, M. Markham, M.E. Newton, et al., Diamond membrane production: the critical role of radicals in the non-contact electrochemical etching of sp2 carbon, Carbon 185 (2021) 717–726.
[11] M. Marchywka, P.E. Pehrsson, S.C. Binari, D. Moses, Electrochemical patterning of amorphous carbon on diamond, J. Electrochem. Soc. 140 (2) (1993) L19.
[12] F.M. Elam, F.C. Hsia, S. van Vliet, R. Bliem, L. Yang, B. Weber, et al., The influence of corrosion on diamond-like carbon topography and friction at the nanoscale, Carbon 179 (2021) 590–599.
[13] O. Sharifahmadian, F. Mahboubi, S. Yazdani, Comparison between corrosion behaviour of DLC and N-DLC coatings deposited by DC-pulsed PACVD technique, Diam. Relat. Mater. 95 (2019) 60–70.
[14] W. Li, D. He, W. Ren, L. Wang, L. Shang, G. Zhang, Tribological behaviors of DLC films in sulfuric acid and sodium hydroxide solutions, Surf. Interface Anal. 52 (7) (2020) 396–406.
[15] S. Tunmee, P. Photongkam, C. Euaruksakul, H. Takamatsu, X. Zhou, P. Wongpanya, et al., Investigation of pitting corrosion of diamond-like carbon films using synchrotron-based spectromicroscopy, J. Appl. Phys. 120 (19) (2016), 195303.
[16] R.W. Coughlin, M. Farooque, Hydrogen production from coal, water and electrons, Nature 279 (5711) (1979) 301–303.
[17] Y.V. Pleskov, Electrochemistry of diamond: a review, Russ. J. Electrochem. 38 (12) (2002) 1275–1291.
[18] J.A. Bennett, J. Wang, Y. Show, G.M. Swain, Effect of sp2-bonded nondiamond carbon impurity on the response of boron-doped polycrystalline diamond thin-film electrodes, J. Electrochem. Soc. 151 (9) (2004) E306.
[19] K.B. Holt, A.J. Bard, Y. Show, G.M. Swain, Scanning electrochemical microscopy and conductive probe atomic force microscopy studies of hydrogen-terminated boron-doped diamond electrodes with different doping levels, J. Chem. Phys. B 108 (39) (2004) 15117–15127.
[20] A.K. Neufeld, A.P. O'Mullane, Effect of the mediator in feedback mode-based SECM interrogation of indium tin-oxide and boron-doped diamond electrodes, J. Solid State Electrochem. 10 (10) (2006) 808–816.
[21] A.L. Colley, C.G. Williams, U. D'Haenens Johansson, M.E. Newton, P.R. Unwin, N. R. Wilson, et al., Examination of the spatially heterogeneous electroactivity of boron-doped diamond microarray electrodes, Anal. Chem. 78 (8) (2006) 2539–2548.
[22] C. Kranz, Diamond as advanced material for scanning probe microscopy tips, Electroanalysis 28 (1) (2016) 35–45.

[23] H.V. Patten, S.C. Lai, J.V. Macpherson, P.R. Unwin, Active sites for outer-sphere, inner-sphere, and complex multistage electrochemical reactions at polycrystalline boron-doped diamond electrodes (pBDD) revealed with scanning electrochemical cell microscopy (SECCM), Anal. Chem. 84 (12) (2012) 5427–5432.
[24] M. Jiang, H. Yu, X. Li, S. Lu, X. Hu, Thermal oxidation induced high electrochemical activity of boron-doped nanocrystalline diamond electrodes, Electrochim. Acta 258 (2017) 61–70.
[25] M.R. Nellist, Y. Chen, A. Mark, S. Gödrich, C. Stelling, J. Jiang, et al., Atomic force microscopy with nanoelectrode tips for high resolution electrochemical, nanoadhesion and nanoelectrical imaging, Nanotechnology 28 (9) (2017), 095711.
[26] N. Hernández-Ibáñez, V. Montiel, J.M. Molina-Jordá, J. Iniesta, Fabrication, characterization and electrochemical response of pitch-derived open-pore carbon foams as electrodes, J. Appl. Electrochem. 48 (3) (2018) 329–342.
[27] R.L. McCreery, Advanced carbon electrode materials for molecular electrochemistry, Chem. Rev. 108 (7) (2008) 2646–2687.
[28] Y. Liu, L. Chen, B. Jiang, Y. Liu, B. Zhang, C. Xiao, et al., Origin of low friction in hydrogenated diamond-like carbon films due to graphene nanoscroll formation depending on sliding mode: Unidirection and reciprocation, Carbon 173 (2021) 696–704.
[29] Z. Ji, Q. Lin, Z. Huang, S. Chen, P. Gong, Z. Sun, et al., Enhanced lubricity of CVD diamond films by in-situ synthetization of top-layered graphene sheets, Carbon 184 (2021) 680–688.
[30] J. Kim, J. Lee, Y. Tak, Relationship between carbon corrosion and positive electrode potential in a proton-exchange membrane fuel cell during start/stop operation, J. Power Sources 192 (2) (2009) 674–678.
[31] Z. Ahmad, Principles of Corrosion Engineering and Corrosion Control, Elsevier, 2006.
[32] E. McCafferty, Validation of corrosion rates measured by the Tafel extrapolation method, Corrosion Sci. 47 (12) (2005) 3202–3215.
[33] J. Wang, J. Zhou, H. Long, Y. Xie, X. Zhang, H. Luo, et al., Tribological, anti-corrosive properties and biocompatibility of the micro-and nano-crystalline diamond coated Ti6Al4V, Surf. Coat. Technol. 258 (2014) 1032–1038.
[34] D. Ballutaud, F. Jomard, T. Kociniewski, E. Rzepka, H. Girard, S. Saada, Sp3/sp2 character of the carbon and hydrogen configuration in micro-and nanocrystalline diamond, Diam. Relat. Mater. 17 (4–5) (2008) 451–456.
[35] J.G. Buijnsters, M. Tsigkourakos, T. Hantschel, F.O. Gomes, T. Nuytten, P. Favia, et al., Effect of boron doping on the wear behavior of the growth and nucleation surfaces of micro-and nanocrystalline diamond films, ACS Appl. Mater. Interfaces 8 (39) (2016) 26381–26391.
[36] A.C. Ferrari, J. Robertson, Resonant Raman spectroscopy of disordered, amorphous, and diamondlike carbon, Phys. Rev. B 64 (7) (2001), 075414.
[37] J.G. Buijnsters, J.P. Celis, R.W. Hendrikx, L. Vázquez, Metallic seed nanolayers for enhanced nucleation of nanocrystalline diamond thin films, J. Chem. Phys. C 117 (44) (2013) 23322–23332.
[38] P.T. Moseley, D.A. Rand, A. Davidson, B. Monahov, Understanding the functions of carbon in the negative active-mass of the lead–acid battery: a review of progress, J. Energy Storage 19 (2018) 272–290.
[39] F. Klauser, S. Ghodbane, R. Boukherroub, S. Szunerits, D. Steinmüller-Nethl, E. Bertel, et al., Comparison of different oxidation techniques on single-crystal and nanocrystalline diamond surfaces, Diam. Relat. Mater. 19 (5–6) (2010) 474–478.
[40] A. Stacey, S. Michaelson, J. Orwa, S. Rubanov, S. Prawer, B. Cowie, et al., Near coalescent submicron polycrystalline diamond films deposited on silicon: hydrogen bonding and thermal enhanced carbide formation, J. Appl. Phys. 106 (10) (2009), 103503.
[41] A.M. Oickle, J. Tom, H.A. Andreas, Carbon oxidation and its influence on self-discharge in aqueous electrochemical capacitors, Carbon 110 (2016) 232–242.
[42] P. Reinke, P. Oelhafen, Electronic properties of diamond/nondiamond carbon heterostructures, Phys. Rev. B 60 (23) (1999), 15772.
[43] A. Denisenko, A. Romanyuk, C. Pietzka, J. Scharpf, E. Kohn, Surface damages in diamond by Ar/O_2 plasma and their effect on the electrical and electrochemical characteristics of boron-doped layers, J. Appl. Phys. 108 (7) (2010), 074901.
[44] M. Walter, F. Mangolini, J.B. McClimon, R.W. Carpick, M. Moseler, Fermi Level Pinning by Defects Can Explain the Large Reported Carbon 1s Binding Energy Variations in Diamond, 2019 arXiv preprint arXiv:190202958.
[45] P. Baumann, R. Nemanich, Surface cleaning, electronic states and electron affinity of diamond (100), (111) and (110) surfaces, Surf. Sci. 409 (1998) 320–335.
[46] A. Dychalska, M. Trzcinski, K. Fabisiak, W. K Paprocki, S. Łoś Koczorowski, et al., The effect of UV and thermally induced oxidation on the surface and structural properties of CVD diamond layers with different grain sizes, Diam. Relat. Mater. 121 (2022), 108739.
[47] K. Fabisiak, M. Kowalska, M. Szybowicz, K. Paprocki, P. Popielarski, A. Wrzyszczyński, et al., The undoped CVD diamond electrode: the effect of surface pretreatment on its electrochemical properties, Adv. Eng. Mater. 15 (2013) 935–940.
[48] C. Goeting, F. Marken, A. Gutiérrez-Sosa, R. Compton, J. Foord, Electrochemically induced surface modifications of boron-doped diamond electrodes: an X-ray photoelectron spectroscopy study, Diam. Relat. Mater. 9 (2000) 390–396.
[49] S. Ferro, A. Battisti, Electron transfer reactions at conductive diamond electrodes, Electrochim. Acta 47 (2002) 1641–1649.